Journal of
Nanotechnology and Smart Materials

JScholar
Fostering Scholarly Communication

Research Open Access

Tuning of WO_3 Phase Transformation and Structural Modification by Reactive Spray Deposition Technology

Rishabh Jain[1, 3, 4,*], Yang Wang[1, 3,4] and Radenka Maric[1, 2, 3]

[1]Department of Materials Science and Engineering, University of Connecticut, 97 North Eagleville Road, Unit 3136 Storrs, CT 06269.
[2]Department of Chemical and Biomolecular Engineering, University of Connecticut, 191Auditorium Road, Unit 3222 Storrs, CT 06269.
[3]Center for Clean Energy Engineering, University of Connecticut, 44 Weaver Road, Unit 5233 Storrs, CT 06269.
[4]Institute of Materials Science, University of Connecticut, 97 North Eagleville Road, Unit 3136 Storrs, CT 06269.

***Corresponding author:** Rishabh Jain, University of Connecticut, Department of Materials Science and Engineering and Center for Clean Energy Engineering, 44 Weaver Road, Storrs, CT 06269–5233, USA. Tel: +1–860–465–6454; fax: +1–860–486–8378; E–mail address: rishabh.jain@uconn.edu

Received Date: February 04, 2014 **Accepted Date:** March 09, 2014 **Published Date:** March 11, 2014

Citation: Rishabh Jain, et al. (2014) Tuning of WO_3 Phase Transformation and Structural Modification by Reactive Spray Deposition Technology. J Nanotech Smart Mater 1: 1-7

Abstract

WO_3 nanoparticle thin films were synthesized by Reactive Spray Deposition Technology (RSDT) by varying the length of the reaction zone (9–14 cm), flow rate of quench air (0–57 L/min) and substrate temperature (80–400 ˚C). The resulting samples were subjected to different annealing conditions (no annealing–500 ˚C). Distinct metastable phases of WO_3 such as ferroelectric ε–WO_3 and the preferential orientation of the three major lattice planes (002), (020) and (200) can be obtained using this synthesis technique and the morphology, and microstructure of the films are a decisive function of the synthesis process. RSDT has a strong potential to allow the properties of WO_3 to be tailored to its desired structure and application. The morphology, structure and size of WO_3 nanoparticles were probed using, X–Ray Diffraction (XRD), Raman spectroscopy, Transmission Electron Microscopy (TEM) with selected area electron diffraction (SAED), and Scanning Electron Microscopy (SEM) with X–Ray Energy Dispersive Spectroscopy (XEDS).

Keywords: WO_3 Thin Film; X–ray Diffraction; Phase Transformation; Preferential Orientation; Reactive Spray Deposition Technology

Introduction

Tungsten oxide (WO_3) thin films have been a subject of extensive scientific investigation following the discovery of WO_3's gas sensing properties (H_2 [1], H_2S [2-8], NO_X [9-12], NH_3[13-18], O_3[19-22], CO[23-26]) and its suitability for use in breath acetone monitors as a tool for non–invasive blood glucose quantification[27-30]. The chromogenic capability of WO_3 in presence of ultra violet light, electric current[31] or gas[32] has created a whole new opportunity for the development of smart windows, optical memory, display devices, etc. Other applications include high energy density microbatteries [33,34], electro–catalysis, optoelectronics, microelectronics, and selective catalysis[35,36]. WO_3 is a semiconductor material known to exist in multiple polymorphs such as tetragonal (α)[37], orthorhombic (β)[38], monoclinic (ε and γ)[39], triclinic (δ)[40,41] and so–called pseudo cubic[42]. Each of these forms exhibits different electrical, optical and magnetic behaviors which are favorable for particular applications. For sensing functions, the WO_3 film needs to be porous and have a large surface area to enable the analytes to diffuse through the film[43]. Acentric nature and spontaneous electric dipole moment of ferroelectric ε–WO_3 leads to increased interaction with high dipole moment analytes such as acetone[44] which is used for medical devices sensing the acetone level in human breath in concentrations of parts per billion (ppb) for non–invasive blood glucose monitoring[29,45]. Photo electrochemical and photo catalytic properties are enhanced when the film is highly crystalline and preferentially oriented in the monoclinic phase because this highly crystalline structure will have fewer defects when acting as the recombination center and should suppress mu-

tual e^-–h^+ recombination[46,47]. Polycrystalline WO_3 film has almost no photochromic sensitivity whereas amorphous WO_3 has high photochromic and electrochromic sensitivity due to high surface area[48,49]. However, some phases of WO_3 such as ε–monoclinic is metastable at room temperature and higher temperature, thereby making it challenging to obtain such phase by the traditional synthesis processes. Here we have demonstrated a one–step flame–based direct deposition technique to engineer a particular required phase by changing the length of the reaction zone in the flame, flow rate of quench air, and the substrate temperature. RSDT is a type of flame spray pyrolysis system which is employed for synthesizing nano scale materials with high efficiency and reduced solvent waste. Here we will give a brief description of the RSDT process and, the conditions required to achieve a particular phase, and we will provide characterization results obtained by Raman spectroscopy, SEM, TEM, and XRD that prove the existence of the phases. The motivation of this research was to study the particle size, crystallinity and crystal structure of the WO_3 films grown by RSDT by varying the conditions of the experiments. It is assumed that the results from this study can be used to obtain the configuration of WO_3 film demanded by its application.

Reactive Spray Deposition Technology

Reactive Spray Deposition Technology (RSDT) was developed by Maric et al. for synthesis of nanoparticle thin films with atomic–level precision and control of properties such as phase, structure, shape, particle size distribution (0.5–100 nm), density and porosity, which can employ a broader selection of precursors compared to conventional vapor–fed flame reactors[50-66]. RSDT is a single–step, open atmosphere flame process for synthesizing nano–materials, whereby nano–particles are synthesized in the reaction zone of the flame and directly deposited on the substrate as a film or collected as particles[50-66], thereby eliminating the intermediate steps of filtration, drying, and calcination. No waste is generated because the solvent is combusted in the flame, yielding CO_2 and H_2O. Precise control of particle size and crystallinity can be achieved by adjusting flame setup conditions, including precursor concentration, chemistry, and flow rate; length of reaction zone; equivalence ratio (stoichiometric oxidant and fuel flow rate to actual oxidant and fuel flow rate); downstream quench air flow rate, and the substrate temperature[53]. In addition to these conditions, flame dynamics is also dependent on the solvent boiling point, enthalpy of combustion of solvent and the combustion nozzle geometry. Results from Roller, et al.[51-52] using RSDT, for Pt based electro-catalysts has clearly shown that the process can be adjusted to give precise control (< 1 nm) on metallic nanoparticle diameters directly deposited onto Nafion® membranes with thickness from ~100 nm to 10 µm. The reactive spray synthesis of nanoparticles relies on combustion of a solvent which also acts as a fuel and aids in the decomposition of a precursor to form nanoparticles. RSDT provides adjustable process variables such as flame temperature, stoichiometry, residence time, and downstream quenching rates that coupled with solvent and metal precursor concentrations, affect particle: nucleation, growth, annealing, and oxidation. Since the droplets produced by this process are mostly sub-micron – due to energetic inputs of heat, pressure, and supercritical propane diluent – the precursor is confined to the nanoscale regime during formation. During the particle formation process the precursor heats up, decomposes, and then undergoes a phase transition to vapor followed by concurrent reduction of the metal ions to metal or metal oxides.

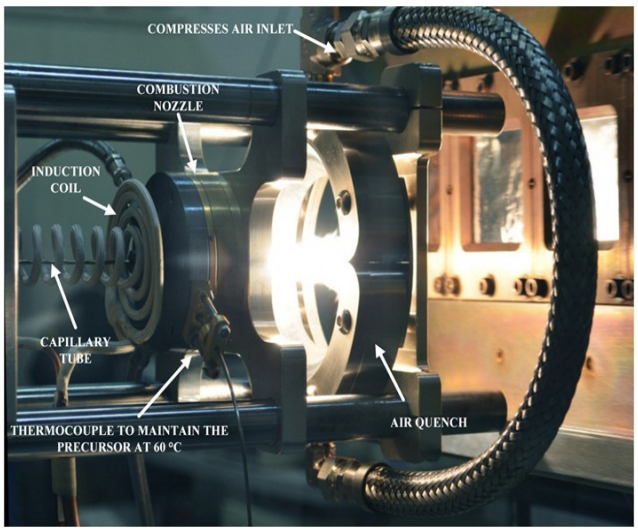

Figure 1. The setup of Reactive Spray Deposition Technology (RSDT)

Experimental

Synthesis of WO_3

An explanation of the RSDT equipment and process is described in detail by Roller, et al.[51] . Tungsten hexacarbonyl ($W(CO)_6$) was obtained from Sigma Aldrich (Catalogue #AC221040100) and was dissolved in a tetrahydrofuran (THF) (Fisher Scientific # SHBD3901V). 20 wt% sulfur free liquefied propane (Airgas catalogue # PRCP350S) was added to the above to form a precursor solution resulting in a final concentration of 5 mM/L $W(CO)_6$, and 16.5 wt% propane. Propane assists in the atomization of the precursors by increasing the enthalpy of the solution mixture and reducing the droplet size due to supercritical expansion. The flow rate of 4 mL/min was maintained by using a syringe pump. The precursor solution was atomized by a gas–assisted external mixing nozzle (combustion nozzle) by oxygen (5 L/min). Six methane–oxygen flamelets (methane and oxygen at 0.5 L/min each) surround the capillary end, which ignites the combustible precursor mist. Prior to atomization, the precursor solution was heated to approximately 50–60 ˚C by enclosing the capillary by a heating coil. The precursor mist was ignited with a propane torch to obtain a bluish–white flame. At approximately 9–14 cm from the flame, a circular air quench (Exair, Super Air Wipe®) with a compressed air flow rate of 28–56 L/min at room temperature was positioned. A stainless steel substrate holder mounted on an x–y–z platform and having the option of water cooling was used for collection of WO_3 particles. On the substrate holder was mounted a zero diffraction background quartz plate (MTI®) on which the film was grown. Quartz was selected for various reasons: it can withstand the high temperature required during in–situ XRD, it can be imaged in an SEM, it does not have an interfering background in a Raman spectrometer, and the film can be scraped off for TEM analysis.

Role of air quench

A schematic of the air quench is shown in figure 2. The air quench is a circular ring with an internal annular chamber. The compressed air at room temperature enters the two nozzles and is directed towards that chamber. The chamber has a narrow ring nozzle through which the air adopts the coanda profile and flows along the angled surface of the air quench. This also creates a low pressure region behind the air quench causing the entrainment of the surrounding air into the primary air stream. A 360˚ cone of cold air is formed which cools the nanoparticles instantly and prevents growth, agglomeration, and sintering, thereby keeping the particle size small and increasing the active surface area. The distance between the combustion nozzle and the air quench is considered the reaction zone and the length of the reaction zone is proportional to the residence time of the nano–particles in the zone. Adjusting the length of the reaction zone and the flow rate of compressed air gives unique conditions to obtain an assortment of phases and structures of WO_3.

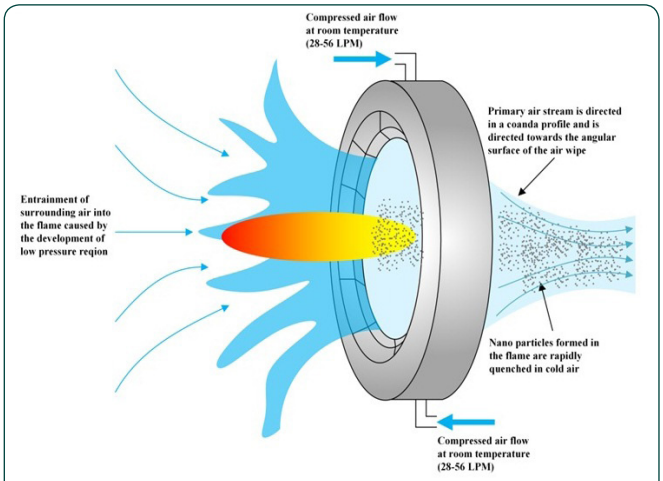

Figure 2. Schematic of air quenching mechanism in RSDT

Characterization

In–situ X–ray diffraction patterns of WO_3 film were recorded in air at 30 ˚C, 150 ˚C, 250 ˚C, 300 ˚C, 350 ˚C, 400 ˚C and 500 ˚C on a Bruker D8 advanced powder diffractometer using CuKα radiation. Heating rate of 5 ˚C /min was used with a hold time of 1 hr at the temperature of the scan. Crystallite size was measured by using Debye Scherrer method. Raman spectra were obtained with a Renishaw Ramascope micro–Raman spectrometer fitted with a reflected light microscope using a 50 mW laser (514.5 nm) and exposure time of 30 s at ambient conditions. Instrument alignment was optimized using a 519 cm^{-1} signal of a silicon wafer. Raman measurements were performed since this technique is well known to give the "fingerprint" of WO_3 material[67]. The spectra were obtained at room temperature in ambient atmosphere in the spectral range between 100 and 1000 cm^{-1}. SEM micrographs were collected on an FEI ESEM Quanta 250 with a field emission gun with an EDAX XEDS system. TEM micrographs and selected area electron diffraction (SAED) pattern of WO_3 particles were obtained on a 120 kV FEI Technai T12 S/TEM with a LaB_6 source equipped with an EDAX XEDS system. 300 mesh Cu grids coated with holey/thin carbon films (Pacific Grid Tech Cu–300HD) were used. A small portion of the film was scraped off from quartz plate and was sonicated with ethanol. Few drops of the resulting solution were dropped on the grids and air dried before they were placed in the UHV chamber of the TEM. The TEM sample was prepared from the crystalline WO_3 film.

Results and Discussion

X–ray diffraction

γ and ε WO_3 with different phase ratio was synthesized in four different set of conditions in RSDT as described in table 1 by altering the length of the reaction zone, flow rate of quench air and temperature of substrate. Figure 3 shows the X–ray diffraction spectra for the samples A, B, C and D. It is clear from the figure that very different structures of WO_3 were obtained by changing the conditions of the flame. All four samples were monoclinic, the most dominant structure of WO_3 and which can be indexed to ICDD#00–043–1035 (space group P21/n). Sample A is the as–prepared sample with no post annealing, and it shows a well crystalline structure with (002) preferential plane oriented at 2θ = 23.1 ˚. This could be due to the high temperature of particles in the absence of quench air which can cause the migration of WO_3 atoms towards the lower energy nucleation sites[68].

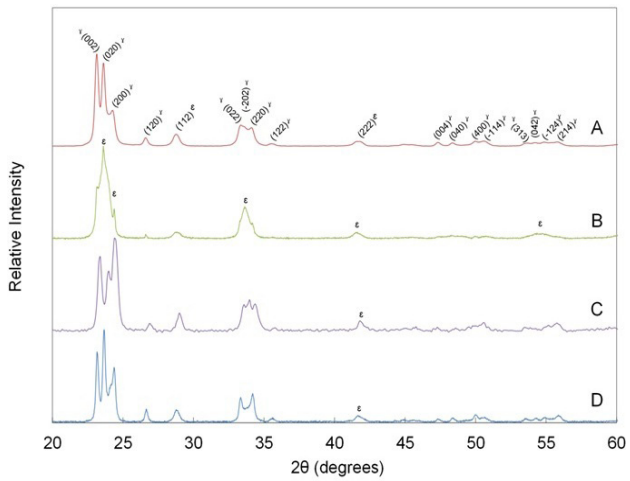

Figure 3. X–ray diffraction of samples A, B, C, and D showing different crystallographic orientations and phase ratio.

All the other samples (with the exception of A) were found to be amorphous in nature because the quench was close to the nucleation site. This amorphous structure could arise because the particles are air quenched as soon as they are produced from the flame and the temperature of the particles and substrate did not exceed 200 ˚C. The amorphous samples were thermally annealed in the high temperature stage of the XRD–the crystallization steps and the corresponding XRD patterns can be found in the supplementary information. Thermal annealing of amorphous WO_3 causes the particles to become crystalline and it also changes the phase ration, grain size, porosity, density of adsorption sites and pore volume[43]. It is clear from in–situ XRD that the crystallization of the WO_3 particles started at 350 ˚C. Sample B was prepared with no air quench; however the substrate temperature was maintained at 200 ˚C by the water cooled substrate holder and the sample thereby retained an amorphous structure. By comparing the XRD pectra of sample B with that of Wang, et al. [29] and Righet-

toni, et al. [45] it can be concluded that the sample is mostly ε–WO_3, the metastable phase at room temperature. Sample C is oriented preferentially along the (200) direction. This preferentially–oriented crystallization was also observed by Sun, et al. [69] and Zhifu, et al. [43] who prepared their films by physical vapor deposition (PVD). Sun et al. suggested that preferential orientation along the (200) direction happened to reduce the lattice mismatch with the sapphire lattice on which the film was grown. According to Zhifu, et al. the cause of this behavior was the column–like accumulation of the WO_3 species during the sputtering process at the operating pressure 20 Pa. The (200) orientation could also form in–situ during the annealing process. Sample D is oriented along the (020) plane direction, and sample A is oriented along the (002) direction, as was also reported by Garavand, et al. [70] Guo, et al. [71] and Jing, et al. [46]. Guo, et al. evaluated the photoelectrochemical activity and photoconversion efficiency of self–assembled nanoporous WO_3 and WO_3 film with preferential orientations at (002) and (020), respectively. They found that the photocurrent of the (002) plane–oriented WO_3 was 9 times the value and the photoconversion efficiency was 4.57 times higher than those of (020) plane–oriented WO_3. Furthermore, (002) WO_3 was more favorable in absorption and redox of pollutants than (020) WO_3. Jing, et al. found that the (002) preferential orientation of WO_3 resulted in higher photocatalytic degradation of NO[46].

Sample	Substrate temperature (°C)	Quench air flow rate (L/min)	Length of reaction zone (nozzle to substrate) (cm)	Preferential plane orientation	Crystallite size (nm)
A	350-400	0	17.1	002	33.1
B	200	0	13.3	NONE	61.6
C	100-130	28.3	20.6	200	29.0
D	80	56.6	12.6	020	42.3

Table 1. Synthesis conditions of WO_3 in Reactive Spray Deposition Technology

Raman Spectroscopy

Figure 4 shows the Raman scattering measurements of untreated sample A and the post–annealed samples B, C and D (since the Raman signal of WO_3 cannot be obtained for amorphous structure).

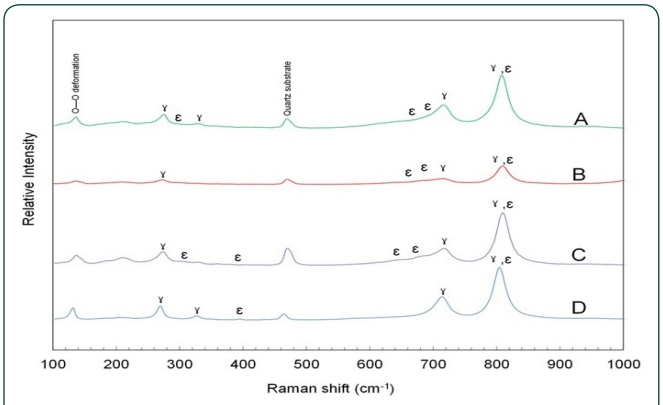

Figure 4. Raman spectroscopy for samples A, B, C, and D showing mostly monoclinic structure.

The spectra are similar to those of the monoclinic WO_3 as apparent from the strong peaks at 808 and 715 cm^{-1}. The peak at 450 cm^{-1} can be assigned to the quartz substrate as determined by the scan of quartz substrate without any film. The intensity of the substrate peak is different for the samples because of the difference in the thickness of the film. A relatively strong peak is obtained at below 150 cm^{-1} for all the samples which can indicate the O–O deformation mode[72]. Salje et al. has obtained the Raman spectra of the monoclinic (γ and ε) WO_3 and is reported in reference[72],[73]. After comparing with Salje, et al. it can be assumed that the peaks at 205, 310, 372, 394, 427, 645, 680, 697cm^{-1} can be assigned to ferroelectric ε–WO_3 while peaks at 327, and 716 cm^{-1} are for γ–WO_3 only. There is clearly an overlap between γ and ε WO_3 as evident from the spectra.

Electron Microscopy

Scanning Electron Microscopy

Figure 5 shows the SEM micrographs of the WO_3 film as deposited (top) and after annealing at 500 °C. Films A and D are very homogeneous while B and C shows particle agglomeration. As is clear from the figure, the size of the grains are in the order B>D>A>C. Pores and cracks can be seen in

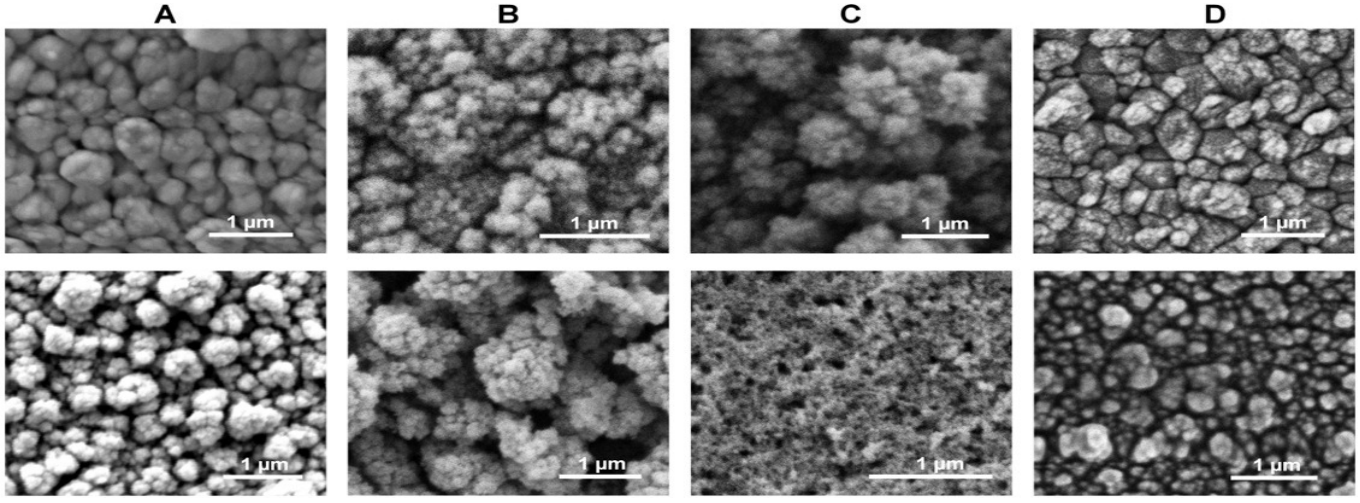

Figure 5. Scanning Electron Microscopy micrographs of WO_3 films deposited by RSDT under condition A, B, C and D. (Top: as deposited, Bottom: after annealing at 500 °C)

samples A and D while samples B and C show uniform morphology. It is interesting to see that in samples A and D, the pores and cracks have grown in size after annealing at 500 ˚C. This same phenomenon was observed by Santato, et al. and could be due to the elimination of organics from the film surface after heat treatment[74]. Increase in porosity of the films is advantageous to the sensing function of WO_3 since this favors diffusion of analytes in the bulk of the film. The images indicate high quality of WO_3 films deposited by RSDT.

Transmission Electron Microscopy

Figure 6 shows the bright field TEM micrographs along with the SAED pattern of samples A–D after post annealing. All samples were polycrystalline, as evident from the SAED pattern

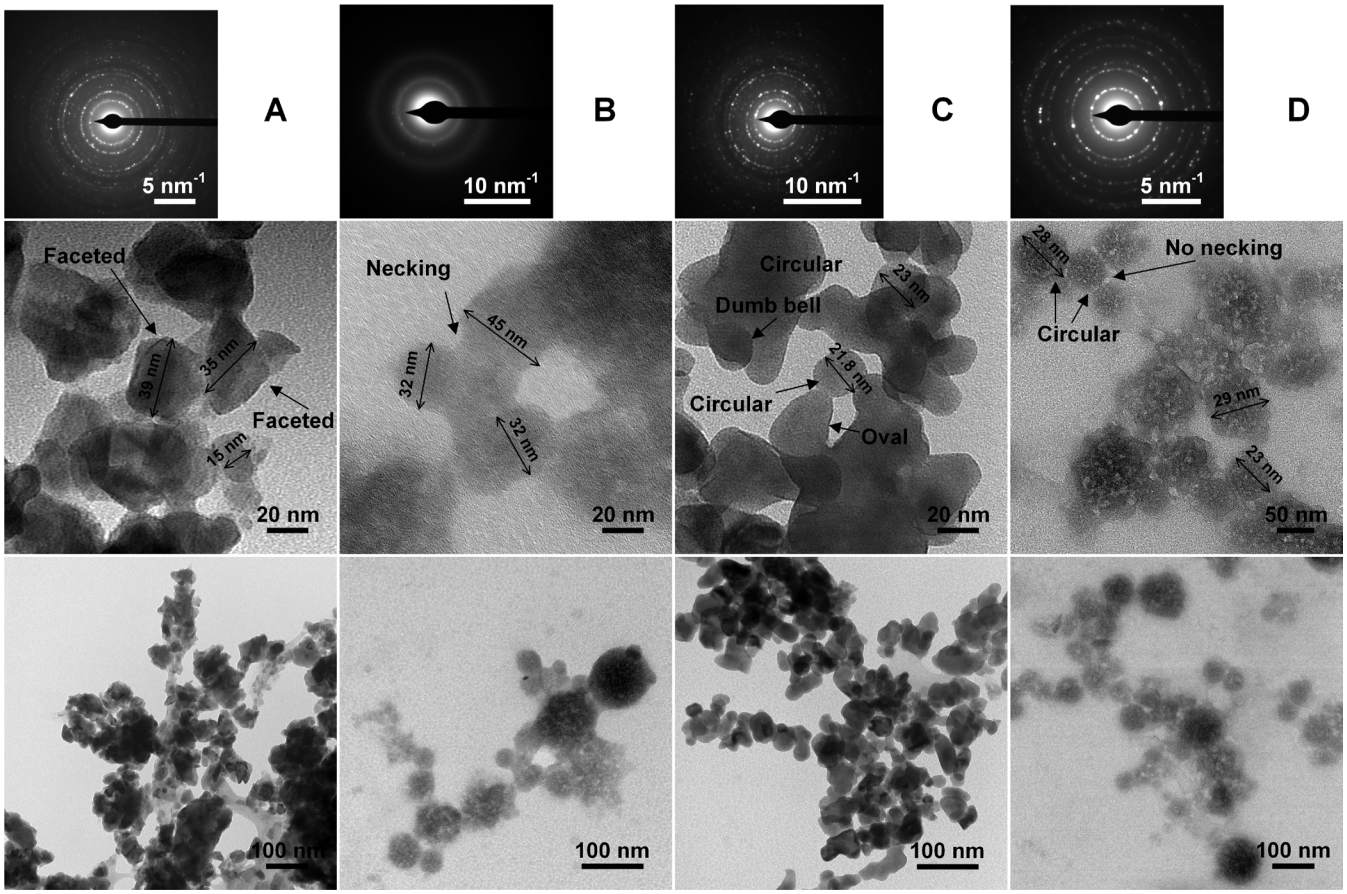

Figure 6. Transmission Electron Microscopy micrographs of WO_3 films deposited by RSDT under conditions A, B, C, and D along with their selected area electron diffraction (SAED) patterns.

and were indexed to monoclinic WO_3. As measured from the micrographs the size of the WO_3 particles were 15–40 nm for sample A, 30–50 nm for sample B, 20–25 nm for sample C, and 20–30 nm for sample D. Different shapes and sizes of particles were seen from the micrographs, as labelled. Sample A shows faceted particles with edges and corners. Samples B and D show circular particles, whereas circular, oval, elliptical, and dumb bell shaped particles can be seen in sample D. Only sample B depicts the formation of necks between individual WO_3 particles.

Conclusions

Reactive Spray Deposition Technology was employed to synthesize WO_3 (γ and ε phase) thin films of from the vapor phase. The morphology, structure and preferential lattice plane orientation was tuned by changing the parameters of the flame set-up including substrate temperature, quench air flow rate and length of reaction zone. It was determined that the particular structure and properties of WO_3 are a function of the synthesis process. By employing the RSDT, the properties of WO_3 can be tuned to be favorable towards a particular application. Our next publication will elaborate upon this technique for exploring the sensing function of WO_3 by changing the synthesis conditions.

Acknowledgements

The authors gratefully acknowledge Ms. Shannon Gagne for help with the experimental setup and data management. This work was financially supported by the school of engineering at University of Connecticut.

References

1) Ahmad MZ, Kang JH, Sadek AZ, Moafi A, Sberveglieri G, et al. (2012) Synthesis of WO_3 Nanorod based Thin Films for Ethanol and H_2 Sensing. Procedia Engineering 47: 358-361.

2) Sun ZY, Yuan HQ, Liu ZM, Han BX, Zhang XR (2005) A highly efficient chemical sensor material for H_2S: α-Fe_2O_3 nanotubes fabricated using carbon nanotube templates. Adv Mater 17: 2993-2997.

3) Kuo LM, Shih Y, Wu C, Lin Y, Chao S, et al. (2013) A new hybrid method for H_2S-sensitive devices using WO_3-based film and ACF interconnect. Meas Sci Technol 24: 075105.

4) Ghimbeu CM, Lumbreras M, Siadat M, Schoonman J (2010) Detection of H_2S, SO_2, and NO_2 using electrostatic sprayed tungsten oxide films. Mat Sci Semicon Proc 13: 1-8.

5) Ionescu R, Hoel A, Granqvist CG, Llobet E, Heszler P (2005) Ethanol and H_2S gas detection in air and in reducing and oxidising ambience: application of pattern recognition to analyse the output from temperature-modulated nanoparticulate WO_3 gas sensors. Sensor Actuat B-Chem 104: 124-131.

6) Szilagyi IM, Saukko S, Mizsei J, Toth AL, Madarasz J, et al (2010) Gas sensing selectivity of hexagonal and monoclinic to H_2S. Solid State Sci 12: 1857-1860.

7) Geng L (2010) Gas sensitivity study of polypyrrole/WO_3 hybrid materials to H_2S. Synth. Met. 160: 1708-1711.

8) Han SD, Singh I, Kim HS, Kim ST, Jung YH, et al. (2002) H_2S gas sensing characteristics of WO_3 thick-films. Indian J Chem A 41: 1832-1836.

9) Ono M, Shimanoe K, Miura N, Yamazoe N (2000) Amperometric sensor based on NASICON and NO oxidation catalysts for detection of total NO_x in atmospheric environment. Solid State Ionics 136: 583-588.

10) Shimizu K, Kashiwagi K, Nishiyama H, Kakimoto S, Sugaya S, et al. (2008) Impedancemetric gas sensor based on Pt and WO_3 co-loaded TiO_2 and ZrO_2 as total NO_x sensing materials. Sensor Actuat B-Chem 130: 707-712.

11) SP Mondal, Dutta PK, Hunter GW, Ward BJ, Laskowski D, et al. (2011) Development of high sensitivity potentiometric NO_x sensor and its application to breath analysis. Sensor Actuat B-Chem 158: 292-298.

12) Ho JJ (2003) Novel nitrogen monoxides (NO) gas sensors integrated with tungsten trioxide (WO_3)/pin structure for room temperature operation. Solid State Electron 47: 827-830.

13) Hieu NV, Le D, Khoang ND, Quy NV, Hoa ND, et al. (2011) A comparative study on the NH_3 gas-sensing properties of ZnO, SnO_2, and WO_3 nanowires. Int J Nanotechnol 8: 174-187.

14) Marquis BT, Vetelino JF (2001) A semiconducting metal oxide sensor array for the detection of NO_x and NH_3. Sensor Actuat B-Chem 77: 100-110.

15) Maciak E, Opilski Z, Pustelny T, Bednorz M (2005) An optical detection NH_3 gas by means of a-WO_3 thin films based on SPR technique. J Phys IV 129: 131-136.

16) Jimenez I, Vila AM, Calveras AC, Morante JR (2005) Gas-sensing properties of catalytically modified WO_3 with copper and vanadium for NH_3 detection. IEEE Sens J 5: 385-391.

17) Srivastava, Jain K (2008) Highly sensitive NH_3 sensor using Pt catalyzed silica coating over WO_3 thick films. Sensor Actuat B-Chem 133: 46-52.

18) Arienzo M D, Armelao L, Mari CM, Polizzi S, Ruffo R, et al. (2011) Macroporous WO_3 Thin Films Active in NH_3 Sensing: Role of the Hosted Cr Isolated Centers and Pt Nanoclusters. J. Am. Chem. Soc. 133: 5296-5304.

19) Guerin J, Bendahan A, Aguir K (2008) . A dynamic response model for the WO_3-based ozone sensors. Sensor Actuat B-Chem 128: 462-467.

20) Qu WM, Wlodarski W (2000) A thin-film sensing element for ozone, humidity and temperature. Sensor Actuat B-Chem 64: 42-48.

21) Labidi A, Gaidi M, Guérin J, Bejaoui A, Maaref M, et al. (2009) Alternating current investigation and modeling of the temperature and ozone effects on the grains and the grain boundary contributions to the WO_3 sensor responses. Thin Solid Films 518: 355-361.

22) Bendahan M, Boulmani R, Seguin JL, Agui K (2004) Characterization of ozone sensors based on WO_3 reactively sputtered films: influence of O_2 concentration in the sputtering gas and working temperature. Sensor Actuat B-Chem 100: 320-324.

23) Al-Kuhaili MF, Durrani SMA, Bakhtiari IA (2010) Carbon monoxide gas-sensing properties of CeO_2-WO_3 thin films. Mater Sci Tech. 26: 726-731.

24) Fukuda H, Zohnishi R, Nomura S (2001) Highly sensitive metal-insulator-semiconductor field-effect transistor sensors for detecting carbon monoxide gas using porous platinum and tungsten oxide thin films. Japanese Journal of Applied Physics 40: 2782-2786.

25) Baraton MI, Merhari L, Ferkel H, Castagnet JF (2002) Comparison of the gas sensing properties of tin, indium and tungsten oxides nanopowders: carbon monoxide and oxygen detection. Mat Sci Eng C-Bio S 19: 315-321.

26) Buono-Core GE, Klahn AH, Cabello G, Muñoz E, Bustamante MJ, et al. (2012) Pt/WO_3 thin films prepared by photochemical metal-organic deposition (PMOD) and its evaluation as carbon monoxide sensor. Polyhedron 41: 134-139.

27) Righettoni M, Tricoli A, Gass S, Schmid A, Amann A, et al. (2012) Breath acetone monitoring by portable Si:WO_3 gas sensors. Anal. Chim. Acta 738: 69-75.

28) Wang L, Kalyanasundaram K, Stanacevic M, Gouma P (2010) Nanosensor Device for Breath Acetone Detection. Sens Lett 8.

29) Wang L, Teleki A, Pratsinis SE, Gouma PI (2008) Ferroelectric WO_3 Nanoparticles for Acetone Selective Detection. Chem. Mater 20: 4794-4796.

30) Righettoni M., Tricoli A, Pratsinis SE (2010) Si:WO_3 Sensors for Highly Selective Detection of Acetone for Easy Diagnosis of Diabetes by Breath Analysis. Anal. Chem 82: 3581-3587.

31) Deb SK (1969) A Novel Electrophotographic System Appl. Opt 8: 192-195.

32) Khoobiar S (1964) Particle to Particle Migration of Hydrogen Atoms on Platinum-Alumina Catalysts from Particle to Neighboring Particles. J. Phys. Chem 68: 411-412.

33) Varella H, Huguenin F, Malta M, Torresi RM (2002) Materiais para cátodos de baterias secundárias de lítio. Quim. Nova 25: 287.

34) Cláudio Trasferetti B, Paulo Rouxinol F, Rogério Gelamo V, Mário Bica de Moraes A (2004) Berreman Effect in Amorphous and Crystalline WO_3 Thin Films. J Phys Chem B 108: 12333-12338.

35) Ma S, Frederick BG (2003) Reactions of Aliphatic Alcohols on WO_3 (001) Surfaces. J Phys Chem B. 107: 11960-11969.

36) Li M, Gao W, Posadas A, Ahn CH, Altman EI (2004) Reactivity of 1-Propanol on p(n×2) Reconstructed WO_3(100) Thin Films. J Phys Chem B 108: 15259-15265.

37) Kehl WL, Hay RG, Wahl D (1952) The Structure of Tetragonal Tungsten Trioxide. J. Appl. Phys 23: 212-215.

38) Salje EKH (1977) The orthorhombic phase of WO_3. Acta Crystallogr B 33: 574.

39) Ekhard Salje KH, Stephan Rehmann, Frank Pobell, Darryl Morris, Kevin S Knight, et al. (1997) Crystal structure and paramagnetic behaviour of ε-WO_3-x. J Phys-Condens Mat 9: 6563.

40) Woodward PM, Sleight AW, Vogt T (1995) Structure refinement of triclinic tungsten trioxide. J Phys Chem Solids 56: 1305-1315.

41) Diehl R, Brandt G, Salje EKH (1978) The crystal structure of triclinic WO_3. Acta Crystallogr B 34.

42) Jiménez I, Arbiol J, Dezanneau G, Cornet A, Morante JR (2003) Crystalline structure, defects and gas sensor response to NO_2 and H_2S of tungsten trioxide nanopowders. Sensors Actuators B: Chem. 93: 475-485.

43) Liu Z, Yamazaki T, Shen Y, Kikuta T, Nakatani N (2007) Influence of annealing on microstructure and NO_2-sensing properties of sputtered WO_3 thin films. Sensor Actuat B-Chem 128: 173-178.

44) Woodward PM, Sleight AW, Vogt T (1997) Ferroelectric Tungsten Trioxide. J Solid State Chem. 131: 9-17.

45) Righettoni M, Tricoli A, Pratsinis SE (2010) Thermally Stable, Silica-Doped ε-WO_3 for Sensing of Acetone in the Human Breath. Chem. Mater 22: 3152-3157.

46) Jing-Xiao Liua b, Xiao-Li Dongb, Xiang-Wen Liua, Fei Shib, Shu Yin, et al. (2011) Solvothermal synthesis and characterization of tungsten oxides with controllable morphology and crystal phase. J. Alloys Compounds 509: 1482-1488.

47) Hiroshi Kominamia,Jun-ichi Katoa, Shin-ya Murakamia, Yoshinori Ishiia, Masaaki Kohno, et al. (2003) Solvothermal syntheses of semiconductor photocatalysts of ultra-high activities. Catalysis Today 84: 181-189.

48) Gavrilyuk AI (1999) Photochromism in WO_3 thin films. Electrochim. Acta 44: 3027-3037.

49) Se-Hee Lee, Hyeonsik Cheong M, Ji-Guang Zhang, Angelo Mascarenhas, David Benson K, et al. (1999) Electrochromic mechanism in a-WO_3−y thin films. Appl. Phys. Lett 74: 242-244.

50) Roller JM, Jiménez MJ, Yu H, Jain J, Carter CB, et ak. (2013) Catalyst nanoscale assembly from the vapor phase on corrosion resistant supports. Electrochim Acta 107: 632-655.

51) Roller JM, Jiménez MJ, Jain R, Yu H, Carter CB, et al. (2013) Processing, Activity and Microstructure of Oxygen Evolution Anodes Prepared by a Dry and Direct Deposition Technique. ECS Trans 45: 97-106.

52) Roller J, Neagu R, Orfino F, Maric R (2012) Supported and unsupported platinum catalysts prepared by a one-step dry deposition method and their oxygen reduction reactivity in acidic media. J Mater Sci 47: 4604-4611.

53) Maric R, Roller J, Neagu R (2011) Flame-Based Technologies and Reactive Spray Deposition Technology for Low-Temperature Solid Oxide Fuel Cells: Technical and Economic Aspects. J Therm Spray Techn 20: 696-719.

54) Maric R, Furusaki K, Nishijima D, Neagu R (2011) Thin Film Low Temperature Solid Oxide Fuel Cell (LTSOFC) by Reactive Spray Deposition Technology (RSDT). ECS Trans 35: 473-481.

55) Nédéleca R, Neagub R, Uhlenbrucka S, Maricc R, Sebolda D, et al. (2011) Gas phase deposition of diffusion barriers for metal substrates in solid oxide fuel cells. Surf Coat Tech 205: 3999-4004.

56) Maric R, Neagu R, Zhang-Steenwinkel Y, Van Berkel FPF, Rietveld B (2010) Reactive Spray Deposition Technology – An one-step deposition technique for Solid Oxide Fuel Cell barrier layers. J Power Sources 195: 8198-8201.

57) Yongsong Xie, Roberto Neagu, Ching-Shiung Hsu, Xinge Zhang, Cyrille Decès-Petit, et al. (2010) Thin Film Solid Oxide Fuel Cells Deposited by Spray Pyrolysis. J Fuel Cell Sci Tech 7: 021007.

58) Khalid Fatih, Roberto Neagu, Vanesa Alazate, Vladimir Neburchilov, Radenka Maric, et al. (2009) Activity of Pt-Sn Catalyst Prepared by Reactive Spray Deposition Technology for Ethanol Electro-oxidation. ECS Trans 25: 1177-1183.

59) Neagu R, Zhang X, Maric R, Roller JM (2009) Characterisation and Performance of SOFC Components made by Reactive Spray Deposition Technology. ECS Trans 25: 2481-2486.

60) Maric R, Roller JM, Neagu R, Fatih K, Tuck A (2008) Low Pt Thin Cathode Layer Catalyst Layer by Reactive Spray Deposition Technology. ECS Trans 12: 59-63.

61) Maric R, Vanderhoek TPK, Roller JM (2008) Reactive Spray Formation of Coatings and Powders. US Patent App 370.

62) Zhenwei Wanga, Rob Huia, Nikica Bogdanovicb, Zhaolin Tangb, Sing Yick, et al. (2007) Plasma spray synthesis of ultra-fine YSZ powder. J Power Sources 170: 145-149.

63) MARIC R, Deces-Petit, Hui , Xinge Z, Ghosh D, et al. (2006) Preparation and Characterization of Nanocrystalline $Ba_2In_2-xMxO_5-\delta$ $(M=Ce,Zr)$. J Electrochem Soc 153: A1505-A1510.

64) Rob Huia, Radenka Marica, Cyrille Decès-Petita, Edward Stylesa, Wei Qu, et al. (2006) Proton conduction in ceria-doped $Ba_2In_2O_5$ nanocrystalline ceramic at low temperature. J Power Sources 161: 40-46.

65) Maric R, Oljaca M, Vukasinovic B, Hunt AT (2004) Synthesis of Oxide Nanopowders in NanoSpray^{SM} Diffusion Flames. Mater Manuf Process 19: 1143-1156.

66) Jain R, Maric R (2014) Synthesis of nano-Pt onto ceria support as catalyst for water–gas shift reaction by Reactive Spray Deposition Technology. Appl Catal A-Gen 475L 461-468.

67) Bittencourt C, Llobet E, Ivanov P, Vilanova X, Correig X, et al. (2004) Ag induced modifications on WO_3 films studied by AFM, Raman and x-ray photoelectron spectroscopy. J Phys D Appl Phys 37: 3383-3391.

68) ZouC YS, Zhang YC, Lou D, Wang HP, Gu L, et al. (2014) Structural and optical properties of WO_3 films deposited by pulsed laser deposition. J. Alloys Compounds 583: 465-470.

69) Hong-Tao Sun, Carlo Cantalini, Luca Lozzi, Maurizio Passacantando, Sandro Santucci, et al. (1996) Microstructural effect on NO_2 sensitivity of WO_3 thin film gas sensors Part 1. Thin film devices, sensors and actuators. Thin Solid Films 287: 258-265.

70) Tahmasebi Garavand N, Mahdavi SM, Iraji zada A, Ranjbar M (2012) The effect of operating temperature on gasochromic properties of amorphous and polycrystalline pulsed laser deposited WO_3 films. Sensor Actuat B-Chem 169: 284-290.

71) Guo Y, Quan X, Lu N, Zhao H, Chen S (2007) High photocatalytic capability of self-assembled nanoporous WO_3 with preferential orientation of (002) planes. Environ. Sci. Technol 41: 4422-4427.

72) Arai M, Hayashi S, Yamamoto K, Kim SS (1990) Raman Studies of Phase-Transitions in Gas-Evaporated WO_3 Microcrystals. Solid State Commun 75: 613-616.

73) Santato C, Odziemkowski M, Ulmann M, Augustynski J (2001) Crystallographically oriented Mesoporous WO_3 films: Synthesis, characterization, and applications. J. Am. Chem. Soc 123: 10639-10649.

74) Salje EKH (1975) Acta Cryst. Lattice dynamics of WO_3. A31: 360-363.